RESEARCH ARTICLE

Key Points:
- The use of multiscale imaging in upscaling petrophysical properties is presented
- We discuss permeability of Opalinus Clay and its critical microstructural control
- Effect of grain size on permeability in shales is discussed

Correspondence to:
L. M. Keller,
kelu@zhaw.ch

Image-Based Upscaling of Permeability in Opalinus Clay

L. M. Keller[1] (ID) **and L. Holzer[1]**

[1]School of Engineering, Zürich University of Applied Sciences, Winterthur, Switzerland

Abstract This paper presents an approach for upscaling permeability in Opalinus Clay from pore scale to a coarser scale, where pores cannot be resolved and where the transport properties are controlled by the geometry of the clay matrix considered as a distinct phase. Microstructures reconstructed from multiscale image data are cellular models with different sizes of basic building blocks, the so-called voxels. Flow simulations were performed on the basis of the grid that is naturally inherent in the coarser-scale image data that were acquired by synchrotron X-ray computed tomography. Thereby, the spatial distribution of permeability at this coarser scale was determined from image data at the pore scale acquired by focused ion beam nanotomography. Then, coarse-scale microstructures with different clay matrix contents were used as input for flow simulations, which allowed predicting the vertical and horizontal bulk permeability at the mesoscale. In agreement with results of other workers, it turned out that vertical (cross-plane) permeability K_v decreases with increasing clay content, which can be explained in that the presence of coarse nonclayey grains increases permeability of the porous clay matrix when compared to a matrix consisting only of fine-grained shales. Mesoscale permeability anisotropy K_h/K_v increases from about 1 to 2 if the clay content increases from 0.2 to 0.9. The predicted permeability behavior is discussed and compared to results from experiments and other predictive models.

1. Introduction

The evaluation procedure whether clay rocks can be used as host rocks for repositories of nuclear waste or as reservoir rocks commonly involves transport modeling to predict the sealing behavior/reservoir quality of porous sedimentary rocks up to the repository/reservoir scale. Clay rock formations such as Opalinus Clay in Switzerland/Germany are multiphase, anisotropic, and compositionally diverse materials, which exhibit different structural features on multiple length scales. In addition, these sedimentary rock formations vary in the relative contents of the fine-grained porous clay matrix and nonclayey mineral grains, which affects petrophysical properties. Therefore, clay rocks are often considered as a binary mixture of a porous clay matrix and nonclayey mineral grains.

Different contents of porous clay matrix likely affect the ability to store and transmit fluids (Revil & Cathles, 1999; Yang & Aplin, 2007). This is supported by the fact that nanoporosity in nonclayey mineral grains (i.e., carbonates) is low and this type of pore space consists of isolated pore objects, which are not connected (Keller, Schuetz, Gasser, et al., 2013). In addition, the presence of nonclayey mineral grains may affect the arrangement of fine-grained clay particles and thus the pore geometry in porous clay matrix (Day-Stirrat et al., 2011; Schneider et al., 2011). In order to understand the influence of nonclayey mineral grains on the fluid transfer in clay rocks, this study uses realistic clay rock microstructure in an approach for image-based upscaling of permeability.

During recent years imaging methods with different spatial resolutions were applied to clay rocks. Recently, Tahmasebi et al. (2015) and Tahmasebi et al. (2016) combined such multiresolution image data related to pore structures in shales, which are characterized by a multiscale morphology (i.e., nanopores and micropores). The resulting synthesized pore models involve small-scale and large-scale pores, and the model size had an edge length ranging between 10 and 30 μm. Here we combine image data that were acquired on the pore scale with mesoscale image data (i.e., hundreds of microns to millimeter scale) where pores cannot be resolved and the structure of the porous clay matrix must be considered as a distinct phase. The approach attempts to bridge the gap between the two different scales and to use information that was extracted on the pore scale as input for property prediction on the mesoscale in a hierarchical upscaling model. Microstructures reconstructed from image data are naturally presented in the form of grid models with the voxel/pixel representing the size of the basic building blocks. Multiscale imaging thus yielded fine- and coarse-scale grid models, and upscaling means that properties of the coarse-scale building blocks are

defined by using petrophysical information (e.g., porosity and permeability) that was extracted from the fine-scale grid models. This allows predicting petrophysical properties at the next higher length scale related to coarse-scale grid models. The basic concept of the approach is not restricted to any rock type, specific property, or length scale. Here we used image data related to Opalinus Clay rock, and we considered permeability as the property to upscale.

2. Imaging Methods and Samples

The results presented here are based on published image data. In order to account for the microstructural variability, the presented upscaling procedure was applied to two samples: (i) a sample from the shaley facies (sample BDR) and (ii) a sample from the sandy facies (sample BWS). Both samples were taken from Opalinus Clay unit at the Mont Terri rock laboratory, Switzerland, and for both samples focused ion beam nanotomography (FIB) and X-ray computed tomography (XCT) tomographic data are available. The rock laboratory is in and alongside the security gallery of the Mont Terri motorway tunnel in northwest Switzerland. Opalinus Clay has a sedimentary age of around 180 Myr and was deposited in a shallow marine basin. After sedimentation the rock unit was subject to two stages of burial with a maximum burial depth of about 1,350 m. Folding of the mountain belt occurred between 10.5 and 3 Myr ago. The Opalinus Clay can be subdivided into three main facies: shaley facies, sandy facies, and carbonate-rich sandy facies. The samples are all taken about 250 m below the surface. The shaley facies of Opalinus Clay typically contains about 60–70 wt % clay minerals, 10–20 wt % carbonate minerals, and 10–20 wt % quartz and accessory constituents such as feldspars, pyrite, and organic carbon. The sandy facies is substantially lower in clay minerals (~30–40 wt %) and contains about 40–50 wt % carbonate minerals and 20–30 wt % quartz and accessory constituents (Nagra, 2002).

In addition to the predictions made by the upscaling approach and in order to provide additional indications regarding the influence of nonclayey mineral grains on the transport properties of clay rocks, we established a relation between the size of nonclayey mineral grains and porosity. Here we included FIB and XCT tomographic data related to three additional samples. One of those samples (sample BHG) was also taken from the shaley facies of Opalinus Clay unit at the Mont Terri rock laboratory. The other two additional samples are from the Schlattingen borehole SLA-1, Switzerland (see Keller et al., 2015). Sample BD-7 is a calcareous marl with a clay content of about 50 wt %, and sample Opa-3 was taken from the Opalinus Clay unit and has a clay content of about 70 wt % (Keller et al., 2015).

All used methods (imaging methods, image processing and characterization, etc.) are described in detail in our previous publications. Here only a short summary is given. For electron microscopy (FIB/scanning electron microscopy (SEM)/transmission electron microscopy (TEM)) analysis the samples need to be dried prior to analysis. Conventional air drying causes artifacts such as the frequently observed desiccation cracks, which can lead to misleading conclusions in terms of transport paths in clay rocks. In addition, freeze drying of moist materials may cause preparation artifacts such as ice formation or surface roughness during mechanical polishing. Special methods such as high-pressure freezing and subsequent freeze drying were used in order to avoid these artifacts (Bachmann & Mayer, 1987; Keller et al., 2011).

For analyzing the geometric properties of the pore space, 3-D information is required. Three-dimensional information can be acquired with FIB-SEM instruments. This tomographic method enables automated serial sectioning and was first described by Holzer et al. (2004). The edge length of the box that can be analyzed with FIB is about 10–15 μm. Typical size of the imaging voxels is around 10 nm. On this length scale, the pore space in the porous clay matrix possesses a certain degree of homogeneity (see Keller, Schuetz, Gasser, et al., 2013 for further discussion). The porosity that can be resolved by FIB corresponds to about 20–30% of the total pore space (see below) (Keller et al., 2011). Smaller pores can be resolved with scanning transmission electron microscopy (STEM) tomography (Keller, Schuetz, Erni, et al., 2013). Regarding electron beam imaging methods, image resolution is linked to sample size, and it turned out that the sample size that can be analyzed with a single STEM tomography realization is too small to provide representative information (Keller, Schuetz, Gasser, et al., 2013). Nevertheless, STEM/TEM provides useful qualitative information, for example, on the size and shape of intraparticle pores as well as on the pore morphology along phase boundaries.

The mesocale microstructure was investigated by using several different XCT instruments at different length scales (Keller, Schuetz, Erni, et al., 2013; Keller et al., 2015). The aim of using tomographic methods at different
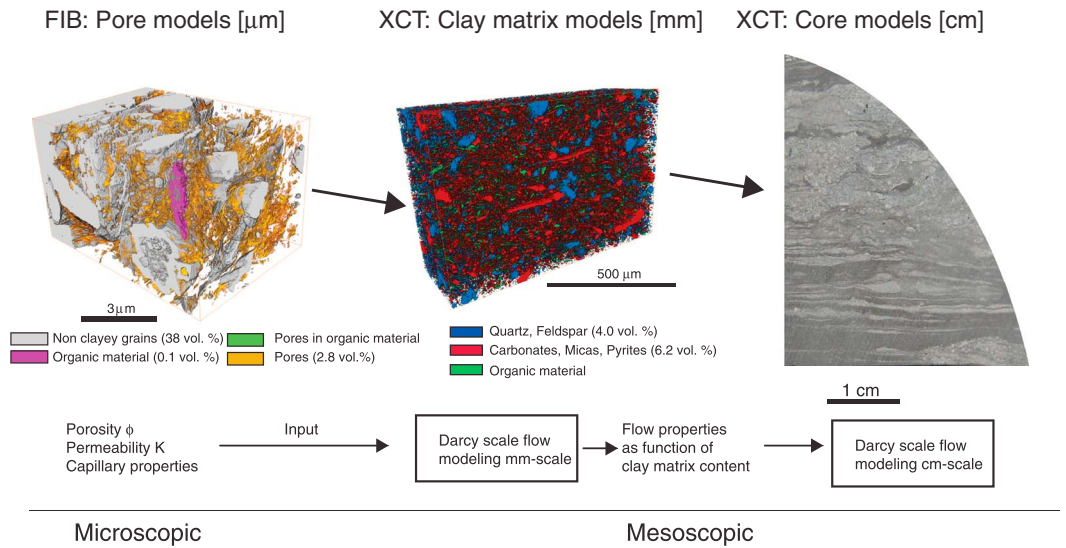
Figure 1. Hierarchy of models that can be used to upscale flow properties. Pore models reconstructed on the basis of FIB image data provide information of porosity and permeability. This information can then be used in clay matrix models that were reconstructed from XCT image data and which are used to calculate flow properties on the millimeter scale. Note that clay is not shown (transparent) in both pore and clay matrix models.

length scales is to establish a hierarchy of models that allows upscaling rock physical properties. The necessary prerequisite for such an approach is the absence of scale gap between particular combinations of tomographic methods. The use of synchrotron XCT at 440 nm image voxel size yielded a scale overlap between the sample size that can be analyzed by FIB and the image voxel size of XCT. In addition, synchrotron XCT produced good image quality, which in combination with proper image processing allowed reconstructing the mesoscale microstructure. Regarding the contents of major constituents, XCT and XRD yielded similar results (Keller et al., 2015). Image processing methods used to process the image stacks acquired by FIB and XCT are described in Keller et al. (2011) and Keller et al. (2015).

3. Multiscale Imaging: A Concept for Image-Based Upscaling

Fluid flow in shales is profoundly affected by compositional variations at different length scales. In general, it is not possible to account with a single model for all factors that affect flow. Instead, one has to develop a series of models, which accounts for specific transport phenomena associated with a limited length of observation. On each length scale one can observe transport paths of different natures, which control flow at the respective length scale. These different transport paths can be visualized and characterized by choosing a tomographic method with suitable resolution range. This is illustrated in Figure 1.

3.1. Microscale

On the microscale, pores can be observed within the clay-rich parts, here referred to as the clay matrix. At this scale, pores are formed due to geometric incompatibities between the grain boundaries of small clay plate-lets. These pores are commonly referred to as intergranular pores, and the radii associated with these pores range from about 2 nm to around 100 nm. In 3-D these pores were imaged using FIB nanotomography, which allowed reconstructing pore microstructures on the tens of micrometer scale (size of image window), with resolutions down to around 10 nm (Figure 2). These pore models can be regarded as the 3-D models of the larger pores because pores with radii <10 nm were not resolved. Regarding these larger pores, the work of Keller, Schuetz, Gasser, et al. (2013) showed that the pore space is characterized by a percolation aniso-tropy related to the bedding. Percolation threshold parallel to bedding was found as low as ~0.04 porosity in the porous clay matrix of the shaley facies and a little higher in the clay matrix of the sandy facies. The measured fraction of larger pores (i.e., radii >~10 nm) is close to or even higher than these values. This implies that percolation through larger pores in the bedding plane is a reasonable assumption. Percolation perpendicular to bedding along larger pores is not very likely because this requires a volume fraction of larger pores
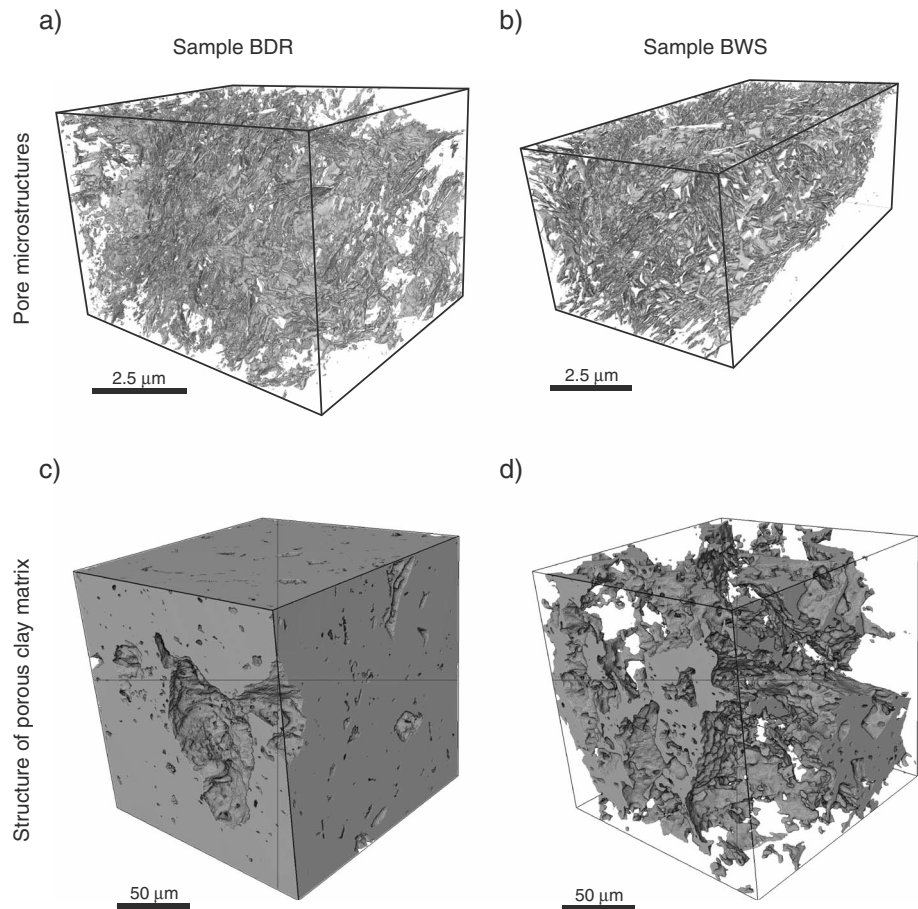
Figure 2. Visualization of the investigated pore microstructures in the porous clay matrix (Figures 2a and 2b) and related microstructures of the clay matrix (Figures 2c and 2d). (a and c) Sample BDR. (b and d) Sample BWS. Figures 2a and 2b = pore models, which were reconstructed from segmented image data that were acquired by FIB nanotomography (approximately 10 nm resolution, clay and nonclayey mineral grains are transparent). Figures 2c and 2d = structural models of clay matrix, which were reconstructed from segmented image that were acquired by XCT (440 nm resolution; porous clay matrix is grey; nonclayey and the impermeable mineral grains are transparent).

higher than ~0.12, which could not be measured with FIB. However, total intergranular porosity (i.e., including Pores with radii ~ < 10 nm) in Opalinus Clay is >~0.12, which in combination with the calculated bulk percolation threshold suggests full connectivity of pore space in Opalinus Clay (Keller, Schuetz, Gasser, et al., 2013). Therefore, we assume that the porosity/permeability relation related to larger pores can be used (i.e., extrapolated) to estimate the permeability beyond the percolation threshold of larger pores where larger pores are connected by smaller pores (see below). The relationship between permeability/porosity related to larger pores as well as the local distribution of larger pores were obtained by repetitive sampling of subvolumes from the total FIB tomography data volume. As shown in Figure 3, the size of the subvolumes (e.g., 440 nm edge length) representing the pore-scale information (from FIB tomography) corresponds to the voxel size of mesoscale models (XCT). In this way the information from multiscale imaging is linked by a single upscaling step.

3.2. Mesoscale

On the mesoscale (i.e., millimeter to centimeter scale), heterogeneities are related to spatially different contents of the porous clay matrix (Figures 1 & 2). Carbonates and quartz are major nonclayey constituents, which were considered as nonpermeable, and thus, the porous clay matrix is heterogeneously distributed on various length scales. Regarding carbonate minerals, this assumption is backed by FIB image data, which revealed that nanopores in carbonates are disconnected and isolated pore objects (Keller, Schuetz, Gasser, et al., 2013). On the mesoscale, fluid flow is controlled by the geometry of the clay matrix (i.e., void
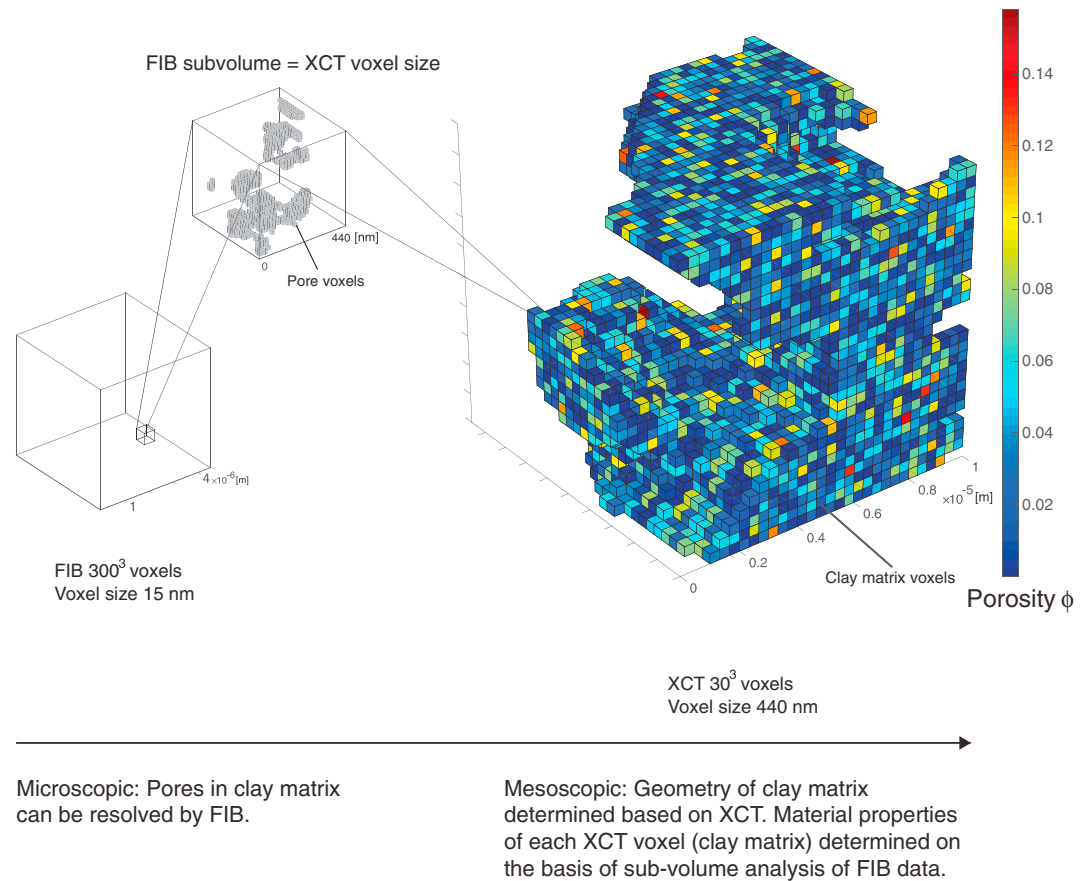
Figure 3. Stages of voxel-based upscaling. Pore models reconstructed from FIB image data were subdivided into regular grid with cell sizes (= subvolume) corresponding to the voxel size in the XCT image data (= 440 nm). All these subvolumes were statistically analyzed, which allowed determining the porosity or other properties for each clay matrix voxel. The colors of the voxels represent the expected porosity in the volume of a specific voxel. This porosity distribution was determined using the local porosity distribution (Figure 4) that was obtained from the statistical analysis.

geometry between nonclayey mineral grains) as well as by the spatial distribution of porosity and permeability inside the clay matrix. On the mesoscale, micropores cannot be resolved by XCT and flow is thus modeled with a macrohomogeneous approach. We used the GeoDict software to solve the Stokes-Brinkman equations for single-phase, incompressible fluid flow (Wiegmann et al., 2010). These equations couple free flow in pores and Darcy flow in a porous media. Thereby, the pores in the porous media cannot be resolved on the scale of the structure under consideration as it is the case for the mesoscale clay matrix. Because the clay matrix of Opalinus Clay is devoid of empty macrospores, the free flow regime can be ignored and the Stokes-Brinkman equation reduces to the Darcy law. Flow modeling on the mesoscale is based on segmented XCT images, which can be regarded as a 3-D grid where each voxel (= grid cell) is allocated to either the clay matrix or nonclayey material. Nonclayey minerals were considered as impermeable (see above). The discretization associated with digital XCT images is then used as input for the computational methods. We used the synchrotron XCT image data with a voxel size of 440 nm that were published in Keller et al. (2015).

In order to perform flow simulations at the mesoscale, the material properties (e.g., flow resistivity) of each of the clay matrix voxels must be defined (= grid properties) (Figure 3). The clay matrix is described by a statistical variation of properties, which represents the variation of pore contents in clay that is observed on the microscale. In particular, the grid properties at the mesoscale were determined at the pore scale by using local porosity theory in combination with pore microstructures that were reconstructed from FIB image data (Biswal et al., 1998; Hilfer, 1991; Hilfer & Helmig, 2004; Hu & Stroeven, 2005; Keller, Schuetz, Gasser, et al., 2013).
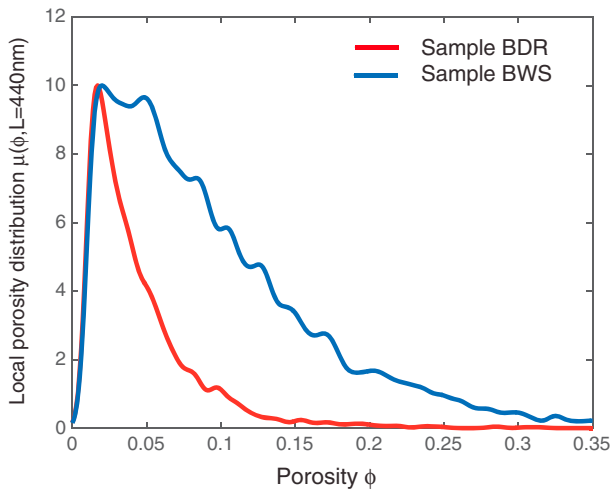
Figure 4. Local porosity distributions, which were calculated by applying local porosity theory to the reconstructed pore microstructures depicted in Figures 2a and 2b and related to the two investigated samples.

3.3. Pore-Scale Properties Used for Upscaling

Here we consider the local porosity distribution of Hilfer (1991) as probability density function (Pdf) of porosity at scale L = 440 nm. This allowed generating random numbers of porosity for each voxel related to mesoscale image data from the distribution specified by the Pdf. The local porosity distribution is defined as

$$\mu(\phi, L) = \frac{1}{m} \sum_{i=1}^{m} \delta(\phi - \phi(x_i, L)), \tag{1}$$

where m is number of placements of measurement cells and $\delta(t)$ denotes the delta function (sometimes called the Dirac delta function). The function $\mu(\phi, L)$ is a measure for the probability to find the local porosity ϕ in a cell with side length L. In addition, we assume homogeneity, which implies that the local porosity distribution related to a specific sample, which was taken from a particular sedimentary facies, does not depend on the location. Regarding the shaley facies of Opalinus Clay this assumption is supported by the finding that similar local porosity distributions were determined for different pore models related to FIB realizations that were performed at different locations (Keller, Schuetz, Gasser, et al., 2013). However, the local porosity distributions depend strongly on L (=cell size). In order to calculate the local porosity distributions, the volume that was analyzed by FIB was subdivided into a cubic grid with a cell size L = 440 nm. Note that this cell size corresponds to the voxel size of the XCT image data (Figure 3). The subdivision into a cubic grid requires that the voxel size of XCT image data must be an integer multiple of the FIB voxel size, which is not the case in case of sample BWS (FIB voxel size was 15 nm). In this case the number of 29.3 FIB voxels was rounded off to the next integer value. The calculated local porosity distributions related to the pore microstructures of the two analyzed samples are displayed in Figure 4. The figure shows that a randomly selected sample from the clay matrix of sample BWS and with an edge length of 440 nm would in an all probability have a higher porosity than a sample of the same size selected form the clay matrix of sample BDR.

Then, the local porosity distributions were used to generate random porosity distributions for each clay matrix voxel of the XCT image stacks (see Figure 3 for illustration). In order to perform flow simulations, the permeability of each cell must be defined, which was done via the porosity/permeability relationship related to a grid length of 440 nm. This relationship was obtained by calculating the permeability for all cells, which percolate in all three directions. The simulations were performed using the GeoDict software, which uses the pore microstructure in form of segmented images data as input and computes a digital flow experiment by solving the Stokes equations for a given pressure drop. In a postprocessing step the relationship between predicted mean flow velocity and pressure drop is used to compute the permeability via Darcy's law. The calculated permeability values depend systematically on porosity, and the relation $\log_{10}(K) = a\phi^b$ was fitted to the data (Figure 5). Using this function in combination with the generated porosity distribution allowed determining the flow resistivity values for flow parallel and perpendicular to bedding of each clay matrix voxel (Figure 6). Flow resistivity is given as viscosity (kg s^{-1} m^{-1}) divided by permeability (m^2). Thereby, we used a value of 0.001 (kg s^{-1} m^{-1}) for the viscosity of water.

4. Results

4.1. Predicting the Mesoscale Permeability

In order to calculate the bulk permeability parallel and perpendicular to bedding, the 3-D flow resistivity distributions related to flow parallel and perpendicular to bedding (Figure 6) were used in combination with the GeoDict software, which solved the Stokes-Brinkman equations (see above). Thereby, a pressure drop of 0.02 Pa was applied parallel and perpendicular to bedding, respectively. This yielded the flow velocity distributions (flow velocity of each voxel). Then, the bulk permeabilities were calculated by averaging the respective velocity vector components along directions parallel and perpendicular to bedding. Thereby, the voxels related to the nonclayey minerals have zero velocity. The obtained mean flow velocities and pressure drop were then used to compute the mesoscale bulk permeabilities for directions parallel and perpendicular to
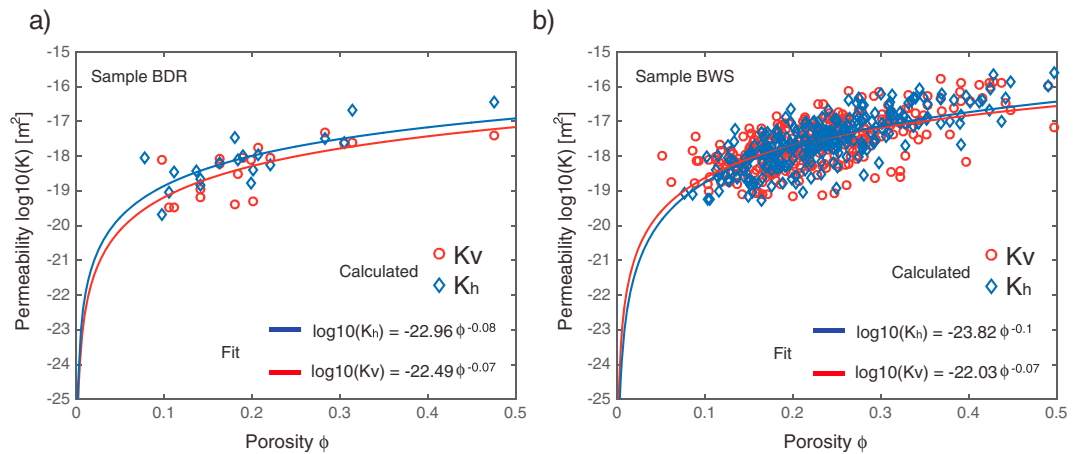
Figure 5. Permeability/porosity relations calculate for (a) sample BDR and (b) sample BWS. Red circles mark calculated permeability values perpendicular to bedding (K_v). Blue diamonds mark calculated permeability values parallel to bedding (K_h). Red and blue lines are curves that were fitted to the calculated values.
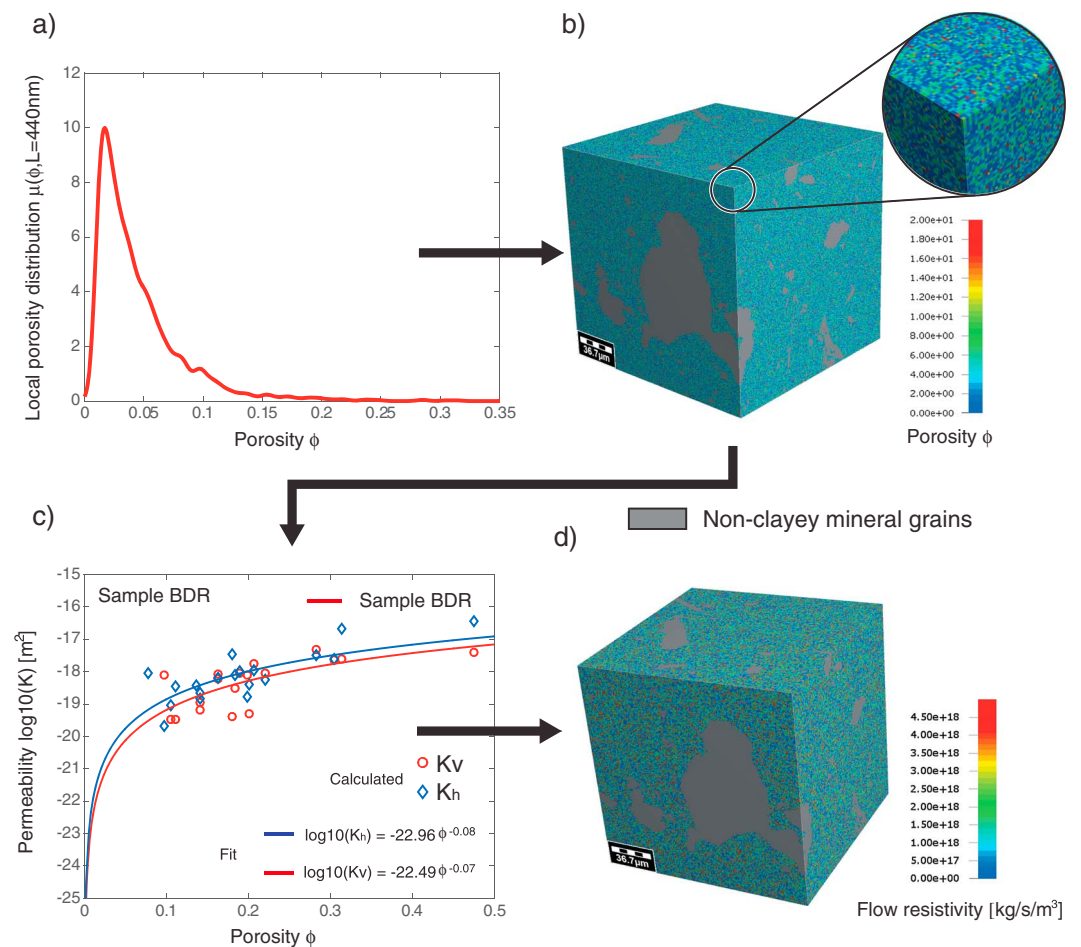

Figure 6. Upscaling procedure. (a) Local porosity distributions were used to determine (b) the porosity of each voxel corresponding to the clay matrix of the mesoscale microstructure. These distributions were then used in combination with (c) permeability/porosity relations in order to determine (d) the flow resistivity of each voxel corresponding to the clay matrix of the mesoscale microstructure. The flow resistivity distributions were then used to calculate the bulk permeability related to the mesoscale microstructures depicted in Figures 2c and 2d.

Table 1
Calculated Mesoscale Permeabilities

Sample	Clay content	Vertical permeability K_v (m^2)	Horizontal permeability K_h (m^2)	Permeability anisotropy K_h/K_v
BDR	0.92	5.1e−21	1.1e−20	2.21
BWS	0.19	3.9e−20	3.3e−20	0.87

bedding via Darcy's law. The mesoscale calculations were done for the clay matrix microstructures depicted in Figure 2. The edge length of the cubes is 176 μm, which corresponds to total of 6.4×10^7 voxels. The calculated permeabilities are documented in Table 1.

The calculations predict a higher permeability for shales with low clay contents (~ clay content of about 0.2) when compared to shales with clay contents as high as 0.9. Because we assumed the nonclayey minerals as nonpermeable, this relation might seem counterintuitive. However, in the present case the clay matrix of the sample with the low clay content has a higher fraction of larger pores when compared to the sample with the high clay content. This is likely because nonclayey minerals of the sample with the low clay content form a grain-supported framework, which affects the compaction state of the clay matrix and, thus, the topology of its pore microstructure. Apparently, this may lead to a comparatively high clay matrix permeability, which substantially increases bulk permeability of low clay content samples even if the majority of the rock constituents (nonclayey minerals) are considered as nonpermeable.

Furthermore, the difference between parallel and perpendicular permeability increases with clay content. Permeability anisotropy increases from 1 to 2 for a clay content increase from 0.2 to 0.9 (Table 1). The reason for this behavior is the fact that the clay matrix of the sample with the high clay content has a higher porosity/permeability anisotropy when compared to the sample with low clay content. Again, this is likely related to differences in compaction state, which leads to a contrast in pore space topology.

4.2. Multiscale Imaging: Impact of Nonclayey Mineral Grains on Porosity in Clay Matrix

Figure 5 suggests that clay matrix porosity alone does not control clay matrix permeability. In order to further investigate the cause of local permeability variations, we established a systematic relationship between grain size distributions of nonclayey minerals and pore size distributions of the porous clay matrix. For this purpose, we considered FIB and synchrotron XCT image data of three additional samples (see above) (Table 2).

For all five samples continuous pore size distributions (Münch & Holzer, 2008) were calculated for given pore microstructures that were reconstructed from FIB image data. Otherwise, discrete grain size distributions (= diameter of spheres having the same volume as the grains) were calculated from FIB and XCT image data. These calculations were done by using the open source image processing platform Fiji in combination with the Xlib plugin (Author B. Muench). As outlined in Keller et al. (2015), XCT allows to distinguish between two

Table 2
Information on Samples Used in This Study

|	Locality	Characteristics of sample location	Method	Sample size (μm^3)	Voxel size (nm)	Porosity (vol %)
BWS H6	Mont Terri Opalinus Clay	Sandy facies	FIB	278	15	7.6 clay matrix
			XCT	4.61e + 07	440	-
BDR_OC 1	Mont Terri Opalinus Clay	Shaley facies	FIB	303	10	2.8 clay matrix
			FIB	331	10	2.3 clay matrix
			XCT	2.85e + 08	440	-
			BET	-	-	11.5
BHG_D1	Mont Terri Opalinus Clay	Shaley facies	FIB	418	10	1.1 clay matrix
			XCT	8.38e + 07	440	-
			BET	-	-	11.5
OPA 3	Schlattingen Opalinus Clay	?	FIB	388	15	0.53 clay matrix
			XCT	1.93e + 08	440	-
BD 7	Schlattingen Braun Dogger	?	FIB	333	10	2.47 clay matrix
			XCT	1.92e + 08	440	-
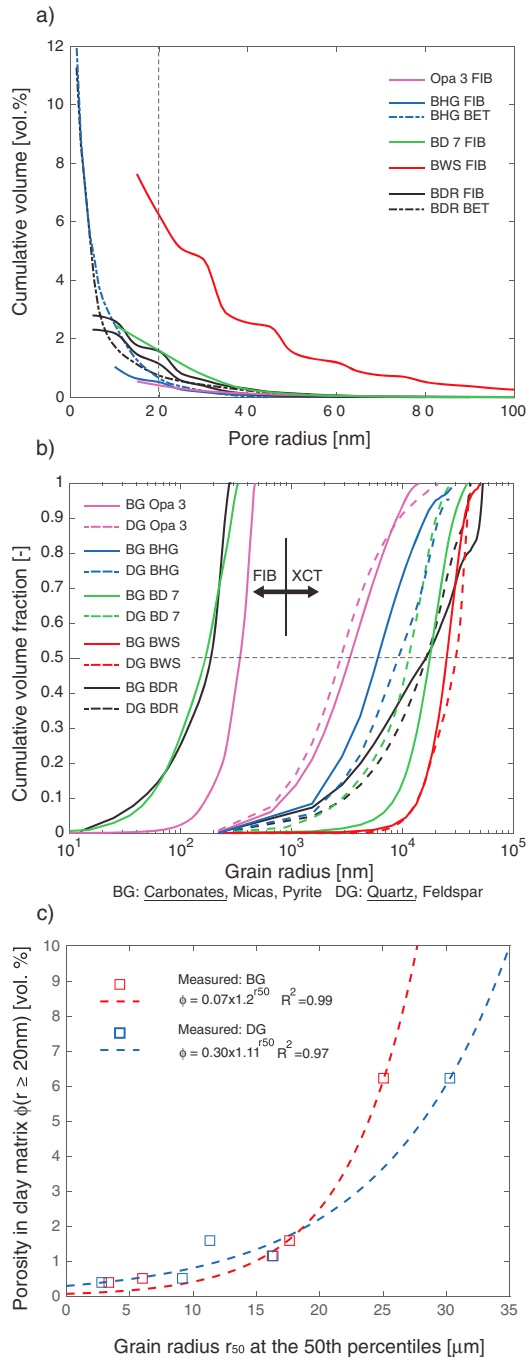
Figure 7. Compilation of (a) pore size and (b) grain size distributions of nonclayey mineral grains calculated on the basis of tomographic image data (FIB and XCT) and the (c) relationship between porosity related to pores with radii ≥ 20 nm and grain size at 50th percentile of nonclayey mineral grains. For a description of the analyzed samples the reader is referred to the text. In Figure 7a the dashed vertical line illustrates the porosity related to pores with radii ≥ 20 nm. In Figure 7b) the dashed horizontal black line through the cumulative volume of 0.5 illustrates the values of the 50th grain size percentile. Grain size distributions were calculated from FIB and XCT image data. This yielded grain size distributions of nonclayey mineral grains for different length scales of observation. For example, the two solid purple lines in Figure 7b are grain size distributions of sample Opa 3, which were obtained on the basis of FIB and XCT image data as indicated by the arrows.

mineral groups that are typically present in the nonclayey mineral fraction of clay rocks: (i) carbonates, micas, and pyrite and (ii) quartz and feldspar. In XCT images, the mineral groups can be distinguished according to their gray level.

Due to different attenuation coefficients, the minerals of the first group appear as bright grains (BG), whereas the minerals of the second group appear as dark grains (DG). They can be distinguished from the clay matrix, which appears at intermediate gray levels. Pore size distributions and grain size distributions are shown in Figure 7. In order to establish a relation between pore size and grain size, the porosity related to pores with radii ≥ 20 nm $\phi(r \geq 20$ nm) were plotted against the grain radii r_{50} at the 50th percentile in the XCT grain size distribution (Figure 7). It turned out that the volume fraction of pores with radii ≥ 20 nm depends on the grain size of the nonclayey minerals. Obviously, the presence of coarse grains leads to a higher volume fraction of larger pores within the clay matrix, which eventually increases clay matrix permeability.

Larger pores are relevant for gas transport because gas flow along smaller pores is hampered due to capillary forces (Clayton & Hay, 1994; Marschall et al., 2005). Hence, gas flow depends largely on the presence of a small volume fraction of larger pores and small changes in the volume fraction of these larger pores can have a substantial impact on the gas transport properties. At least from the qualitative point of view, these transport properties can be estimated if the content of nonclayey mineral grains and the grain size distribution are known.

5. Discussion

The implications of the presented upscaling approach on permeability of Opalinus Clay and shales in general are discussed. First, our approach gives new insight into the microstructural control of permeability of shales. Pore-scale permeability is in part controlled by microstructural features that can be observed at the next longer-length scale. In case of Opalinus Clay these features are related to the framework that is composed of nonclayey mineral grains. This framework likely controls the compaction state (i.e., porosity) of the porous clay matrix that fills the void between nonclayey mineral grains. Hence, spatial variations of the nonclayey mineral content likely affect local pore-scale permeability. Therefore, image-based upscaling of shale properties requires a multiscale microstructural analysis of different clay rock facies.

In addition, the experimental determination of shales permeabilities is difficult and time consuming, which is the reason why models are used to predict permeability on larger scales. Often, these models depend on several parameters such as pore size and pore throat distributions, which generally are not available regarding their variability over larger scales. On the contrary, the presented approach predicts the mesoscale permeability as a function of a single parameter, which is the clay content. Knowing the spatial distribution of the clay content at larger scales (e.g., log scale), the approach might be used to define the permeability distribution at the macro scale. However, the present the data basis is not sufficient for such an upscaling to the log or basin scale and should therefore be improved.

Next we summarize the presented concept for upscaling flow properties that is based on multiscale imaging. Flow simulations were performed on the basis of the grid that is naturally inherent in the coarse-scale image data and which is defined by the voxel resolution of XCT. In order to calculate mesoscale permeability, the coarse-scale spatial distribution of permeability/flow resistivity was determined by using the local porosity distribution in combination with the calculated permeability/porosity relation, which are both coupled to the voxel size L of the coarse image data (Figures 3 and 6). The local porosity distribution and the permeability/porosity relation, in turn, were determined from the fine-scale image data, the pore scale. Distributions and probabilities of pore-scale or microscale properties are obtained by statistical analysis using repetitive sampling of subvolumes from the total FIB-tomography data volume. Thereby, the size of subvolumes (e.g., 440 nm edge length) in the microscale models (FIB tomography) corresponds to the voxel size of mesoscale models (XCT). In this way the information from multiscale imaging is linked by a single upscaling step. Then, flow simulations were applied to measured coarse-scale microstructures with different clay matrix contents, which allowed predicting the mesoscale permeability parallel and perpendicular to bedding for samples with different clay matrix contents (Table 1). It should be noted that the model predictions do not depend on a single porosity and permeability distributions but instead are based on different distributions related to different lithologies (clay contents) and, thus, account for variations in the influence of nonclay grains on the pore structure within the porous clay matrix.

Regarding Opalinus Clay, the calculated permeability values are in good agreement with experimentally derived permeability values, which are on the order of 1e−21 to 1e−20 (m^2) (Marschall et al., 2005). The calculations predict that vertical and horizontal permeability decrease with increasing clay matrix content. Regarding vertical permeability this result is in line with the results presented by Yang and Aplin (2007) and Dewhurst et al. (1999). Furthermore, the presented predictions are in quantitative agreement with Schneider et al. (2011), who report an increase in vertical permeability by 1 order of magnitude if clay contents decrease from 0.57 to 0.36. According to some of the latter authors, coarse-grained shales have larger pore throats when compared to fine-grained shales, which leads to a higher vertical permeability. These interpretations are in good agreement with our results concerning the relationship between porosity and grain size (Figure 7c). The presence of coarse-grained nonclayey mineral apparently increases volume fraction of pores with radii >~20 nm. The higher fraction of relatively large pores within the clay matrix of sandy shales apparently increases vertical bulk permeability, in comparison to clay-rich shales. Hence, the crucial quantity that controls permeability is the porosity in clay matrix rather than the bulk porosity of the clay sand/silt mixture.

Increasing the clay content from about 0.2 to 0.9 is associated with an increase of permeability anisotropy K_h/K_v from around 0.9 to 2.2 (Table 1). This is likely related to differences in compaction state where the matrix of clay-rich shales is expected to be compacted more. Compaction state of the clay matrix is likely affected by the presence of nonclayey grains. This is evidenced by the relationship between porosity and grain size of nonclayey minerals (Figure 7), which implies that the presence of coarse-grained nonclayey minerals increases the volume fraction of larger pores (see also Yang & Aplin, 2007). The calculated permeability anisotropy is in agreement with measured values. Adams et al. (2013) measured the permeability on resedimented Boston Blue Clay, which has clay content of 0.53, and stated that the permeability anisotropy of mechanically compressed mudrocks with platy particles is typically in the range of ~1–2.5 over a stress range of 10 MPa. Clennell et al. (1999) showed that the permeability anisotropy increases from 1.1 to 3 for remolded pure clays, synthetic clays, and natural clays. The experiments of Yang and Aplin (2007) yielded permeability anisotropies up to 11.

6. Conclusions

In this study we used multiscale 3-D tomographic image data related to shale microstructures in an attempt to upscale the permeability of Opalinus Clay. Thereby, transport relevant properties such as local porosity distributions and permeability/porosity relations were extracted at the pore scale. This information was then used at the next higher length scale (= mesoscale) were pores cannot be resolved and the geometry of the porous clay matrix controls transport properties. Then, mesoscale permeabilities were calculated using XCT image data as input. The calculated permeabilities are in agreement with experimentally derived values. In addition, the calculations indicated that permeability decreases with increasing clay content. This result

can be explained by the presence of local permeability contrasts between the porous clay related to shales that are characterized by different clay contents. Hence, local differences in the pore microstructure largely control bulk permeability on the mesoscale. Permeability anisotropy increases from about 1 to 2 if the clay content increases from 0.2 to 0.9.

References

Adams, A. L., Germaine, J. T., Flemings, P. B., & Day-Stirrat, R. J. (2013). Stress induced permeability anisotropy of resedimented Boston Blue Clay. *Water Resources Research*, *49*, 6561–6571. https://doi.org/10.1002/wrcr.20470

Bachmann, L., & Mayer, E. (1987). Physics of water and ice: Implications for cryofixations. In R. A. Steinbrecht & K. Zierold (Eds.), *Cryotechniques in Biological Electron Microscopy* (pp. 3–34). Berlin: Springer. https://doi.org/10.1007/978-3-642-72815-0_1

Biswal, B., Manwart, C., & Hilfer, R. (1998). Three-dimensional local porosity analysis of porous media. *Physica A*, *255*(3-4), 221–241. https://doi.org/10.1016/S0378-4371(98)00111-3

Clayton, C. J., & Hay, S. J. (1994). Gas migration from accumulation to surface. *Bulletin of the Geological Society of Denmark*, *41*, 12–23.

Clennell, M. B., Dewhurst, D. N., Brown, K. M., & Westbrook, G. K. (1999). Permeability of consolidated clays. *Geological Society: Special Publications*, *158*(1), 79–96. https://doi.org/10.1144/GSL.SP.1999.158.01.07

Day-Stirrat, R. J., Schleicher, A. M., Schneider, J., Flemings, P. B., Germaine, J. T., & van der Pluijm, B. A. (2011). Preferred orientation of phyllosilicates: Effects of composition and stress on resedimented mudstone fabric. *Journal of Structural Geology*, *33*, 1347–1358. https://doi.org/10.1016/j.jsg.2011.06.007

Dewhurst, D. N., Aplin, A. C., & Sarda, J.-P. (1999). Influence of clay fraction on pore-scale properties and hydraulic conductivity of experimentally compacted mudstones. *Journal of Geophysical Research*, *104*(B12), 29,261–29,274. https://doi.org/10.1029/1999JB900276

Hilfer, R. (1991). Geometric and dielectric characterization of porous media. *Physics Review*, *44*(1), 60–75. https://doi.org/10.1103/PhysRevB.44.60

Hilfer, R., & Helmig, R. (2004). Dimensional analysis and upscaling of two phase flow in porous media with piecewise constant heterogeneities. *Advances in Water Resources*, *27*, 1033–1040. https://doi.org/10.1016/j.advwatres.2004.07.003

Holzer, L., Indutnyi, F., Gasser, P., Münch, B., & Wegmann, M. (2004). Three-dimensional analysis of porous BaTiO$_3$ ceramics using FIB nanotomography. *Journal of Microscopy*, *216*, 84–95. https://doi.org/10.1111/j.0022-2720.2004.01397.x

Hu, J., & Stroeven, P. (2005). Local analysis of pore structure in cement paste. *Cement and Concrete Research*, *35*, 233–242. https://doi.org/10.1016/j.cemconres.2004.06.018

Keller, L. M., Holzer, L., Wepf, R., & Gasser, P. (2011). 3D geometry and topology of pore pathways in Opalinus Clay: Implications for mass transport. *Applied Clay Science*, *52*, 85–95. https://doi.org/10.1016/j.clay.2011.02.003

Keller, L. M., Schuetz, P., Erni, R., Lucas, F., Gasser, P., & Holzer, L. (2013). Characterization of multi-scale microstructural features in Opalinus Clay. *Microporous and Mesoporous Materials*, *179*, 83–94.

Keller, L. M., Schuetz, P., Gasser, P., & Holzer, L. (2013). Pore-space relevant for gas-permeability in Opalinus Clay: Statistical analysis of homogeneity, percolation and representative volume element. *Journal of Geophysical Research: Solid Earth*, *118*, 2799–2812 https://doi.org/10.1002/jgrb.50228

Keller, L. M., Hilger, A., & Manke, I. (2015). Impact of sand content on solute diffusion in Opalinus Clay. *Applied Clay Science*, *134*, 134–142.

Marschall, P., Horseman, S., & Gimmi, T. (2005). Characterisation of gas transport properties of the Opalinus Clay, potential host rock formation for radioactive waste disposal. *Oil & Gas Science and Technology*, *60*(1), 121–139. https://doi.org/10.2516/ogst:2005008

Münch, B., & Holzer, L. (2008). Contradicting geometrical concepts in pore size analysis attained with electron microscopy and mercury intrusion. *Journal of the American Ceramic Society*, *91*, 4059–4067. https://doi.org/10.1111/j.1551-2916.2008.02736.x

Nagra (2002). Projekt Opalinuston Synthese der geowissenschaftlichen Untersuchungsergebnisse. Entsorgungsnachweis fuer abgebrannte Brennelemente, verglaste hochaktive sowie langlebige mittelaktive Abfaelle (Nagra Technical Report NTB 02–03). Nagra, Wettingen, Switzerland.

Revil, A., & Cathles, L. M. (1999). Permeability of shaley sands. *Water Resources Research*, *35*(3), 651–662. https://doi.org/10.1029/98WR02700

Schneider, J., Flemings, P. B., Day-Stirrat, R. J., & Germaine, J. T. (2011). Insights into pore-scale controls on mudstone permeability trough resedimentation experiments. *Geology*, *39*, 1011–1014. https://doi.org/10.1130/G32475.1

Tahmasebi, P., Javadpour, F., & Sahimi, M. (2015). Multiscale and multiresolution modeling of shales and their flow and morphological properties. *Scientific Reports*, *5*(1), 16373. https://doi.org/10.1038/srep16373

Tahmasebi, P., Javadpour, F., Sahimi, M., & Piri, M. (2016). Multiscale study for stochastic characterization of shale samples. *Advances in Water Resources*, *89*, 91–103. https://doi.org/10.1016/j.advwatres.2016.01.008

Wiegmann, A., Iliev, O., & Schindelin, A. (2010). Computer aided engineering of filter materials and pleated filters. In *Global Guide of the Filtration and Separation Industry* (pp. 191–198). Roedermark, Germany: E. von der Luehe. VDL Verlag.

Yang, Y., & Aplin, A. C. (2007). Permeability and petrophysical properties of 30 natural mudstones. *Journal of Geophysical Research*, *112*, B03206. https://doi.org/10.1029/2005JB004243